

RSC Applied Interfaces

Accepted Manuscript

This article can be cited before page numbers have been issued, to do this please use: Y. Wu and W. Yue, *RSC Appl. Interfaces*, 2026, DOI: 10.1039/D6LF00021E.



This is an Accepted Manuscript, which has been through the Royal Society of Chemistry peer review process and has been accepted for publication.

Accepted Manuscripts are published online shortly after acceptance, before technical editing, formatting and proof reading. Using this free service, authors can make their results available to the community, in citable form, before we publish the edited article. We will replace this Accepted Manuscript with the edited and formatted Advance Article as soon as it is available.

You can find more information about Accepted Manuscripts in the [Information for Authors](#).

Please note that technical editing may introduce minor changes to the text and/or graphics, which may alter content. The journal's standard [Terms & Conditions](#) and the [Ethical guidelines](#) still apply. In no event shall the Royal Society of Chemistry be held responsible for any errors or omissions in this Accepted Manuscript or any consequences arising from the use of any information it contains.

ARTICLE

Multifunctional Fluorine-Nitrogen Modified Carbon Quantum Dots for Enhanced Solid Polymer Electrolytes Toward Solid-State Lithium Batteries

Yang Wu,^a Wenbo Yue^{*a}Received 00th January 20xx,
Accepted 00th January 20xx

DOI: 10.1039/x0xx00000x

Solid polymer electrolytes (SPEs) are pivotal for developing all-solid-state lithium batteries due to their enhanced safety, but their practical application is hindered by low ionic conductivity. Herein, fluorine-nitrogen modified carbon quantum dots (FNCDs) are designed and prepared as a multifunctional filler to overcome this limitation. The FNCDs provide abundant sites for Li⁺ transport and immobilize anions (TFSI⁻), promoting Li salt dissociation. Moreover, the fluorinated surface ensures excellent compatibility with the fluorinated polymer matrix (PVDF-HFP), facilitating favorable interfacial Li⁺ hopping channels. Consequently, the FNCDs-incorporated SPE (FNCDs-SPE) film achieves a high ionic conductivity of 9.59×10^{-4} S cm⁻¹ and a Li⁺ transference number of 0.77. It also exhibits enhanced mechanical strength (3.53 MPa) and elasticity (249.2% elongation). When paired with LiFePO₄, LiCoO₂, or NCM811 cathodes, the corresponding solid-state cells demonstrate exceptional cycling stability. This work highlights the great potential of zero-dimensional fluorinated carbon materials in developing high-performance SPEs.

1 Introduction

With the growing demand for high safety and high energy density in electric vehicles and renewable energy storage, conventional lithium-ion batteries, which rely on flammable liquid electrolytes and graphite anodes, have become increasingly inadequate. In traditional lithium-ion batteries, the flammable liquid electrolytes not only pose significant thermal runaway risks and serious safety hazards but also exhibit restricted compatibility with high-energy lithium metal anodes.^{1,2} Consequently, solid-state lithium metal batteries (SSLMBs) have garnered considerable research interest in recent years.³⁻⁵ The electrolyte, as a critical component, plays a pivotal role in realizing battery systems with high safety and energy density. Although solid-state electrolytes (SSEs) can mitigate safety concerns, they face intrinsic challenges including lower ionic conductivity, poor interfacial contact, stringent fabrication requirements, and higher cost compared to their liquid counterparts.⁶⁻⁹ Overcoming these challenges is therefore imperative for the advancement of SSLMBs.

In response to these challenges, extensive research efforts have been devoted to developing various SSE material systems. The mainstream SSE material systems primarily include inorganic solid electrolytes (ISEs), organic solid polymer electrolytes (SPEs), and composite polymer electrolytes (CPEs). While ISEs (e.g., oxides, sulfides, and halides) typically exhibit high ionic conductivity (10^{-4} to 10^{-2} S cm⁻¹), they often suffer from poor interfacial contact, sensitivity to moisture/oxygen in the air, high cost, and poor

processability, which severely hinder their practical application.^{10,11} In contrast, SPEs have emerged as promising candidates for practical large-scale production owing to their excellent flexibility, good interfacial compatibility, facile processability, and cost-effectiveness.¹²⁻¹⁴ However, commonly studied SPEs based on polymers like polyethylene oxide (PEO), poly(vinylidene fluoride) (PVDF), polyacrylonitrile (PAN), and poly(methyl methacrylate) (PMMA) generally suffer from low ionic conductivity (typically 10^{-7} to 10^{-5} S cm⁻¹) and narrow electrochemical stability windows, which constitute the core challenges for their development.^{15,16} Nevertheless, significant improvements in both ionic conductivity and electrochemical stability have been achieved through strategies such as polymer matrix modification or the incorporation of inorganic fillers. For instance, Cao et al. synthesized cellulose phthalate (CP) via homogeneous esterification, and the corresponding CP-based SSE achieved a high ionic conductivity of 1.09 mS cm⁻¹ and a Li⁺ transference number of 0.81 at room temperature. This enhancement is attributed to the introduced phthalate groups, which enable multiple coordination with Li⁺ and establish a stable conduction network.¹⁷ Similarly, Ahn et al. developed a composite electrolyte (PLiZ) by incorporating ZIF-67 and an ionic liquid (ILE) into a PEO matrix, which achieved an ionic conductivity of 1.19×10^{-4} S cm⁻¹ and a Li⁺ transference number of 0.8 at room temperature. The fillers shortened Li⁺ transport pathways and immobilized anions, thereby enhancing battery performance.¹⁸ These examples underscore the considerable potential of composite strategies for advancing SPEs.

In pristine (unfilled) SPEs, lithium-ion transport primarily relies on the segmental motion of polymer chains. Ionic conduction occurs predominantly in the amorphous regions, whereas it is highly restricted in the crystalline regions due to the tightly packed and ordered polymer chains.¹⁹ Therefore, rational polymer structural

^a Beijing Key Laboratory of Energy Conversion and Storage Materials, College of Chemistry, Beijing Normal University, Beijing 100875, P. R. China.

*E-mail: wbyue@bnu.edu.cn (W.B. Yue)

Supplementary Information available: See DOI: 10.1039/x0xx00000x



design is crucial for facilitating efficient Li⁺ transport. Poly(vinylidene fluoride-co-hexafluoropropylene) (PVDF-HFP) is a copolymer formed with vinylidene fluoride (VDF) and hexafluoropropylene (HFP) monomers. The VDF segments provide a high dielectric constant to promote lithium salt dissociation and confer mechanical robustness, while the HFP segments introduce structural defects that disrupt the regularity of PVDF chains and increase the amorphous phase content. This synergy creates a favorable environment for Li⁺ transport.^{20,21} Beyond polymer design, the incorporation of inorganic fillers is equally critical for enhancing SPE performance. Carbon quantum dots (CDs), a class of zero-dimensional carbon nanomaterials featuring abundant and tunable surface functional groups, have attracted significant research attention.²²⁻²⁵ Their surfaces are typically rich in functional groups such as hydroxyl (-OH), carboxyl (-COOH), and amino (-NH₂). These groups facilitate uniform dispersion within polymer matrices, interact with polymer chains to suppress crystallinity, and provide additional sites for ion transport. Furthermore, the rich surface chemistry of CDs can positively influence electrolyte mechanical properties and interfacial stability with electrodes. Therefore, the rational design and modification of inorganic fillers like CDs are of great importance for constructing fast and stable Li⁺ transport channels and optimizing interfacial compatibility within polymer electrolyte systems.

In this work, we developed a high-performance, flexible solid polymer electrolyte film (denoted as FNCDs-SPE) by incorporating fluorine-nitrogen modified carbon quantum dots (FNCDs) into a PVDF-HFP matrix. The abundant surface functional groups on FNCDs enable their excellent dispersion within the polymer matrix and prevent performance degradation caused by agglomeration. Simultaneously, they disrupt the ordered arrangement of PVDF-HFP chains, thereby increasing the amorphous region content, which is beneficial for ion transport. Notably, the fluorine- and oxygen/nitrogen-containing functional groups on the FNCDs can engage in Lewis acid-base interactions with Li⁺, promoting lithium salt dissociation and providing additional hopping sites for Li⁺ transport. The resulting rapid ion conduction facilitates uniform lithium deposition/stripping, suppresses lithium dendrite growth, and enhances the interfacial stability. Moreover, FNCDs act as physical cross-linking points to entangle and interact with PVDF-HFP molecular chains, which significantly improves the mechanical robustness of the electrolyte. As a result, FNCDs-SPE exhibits a high ionic conductivity of 9.59×10^{-4} S cm⁻¹ and a tensile strength of 3.53 MPa, which are competitive among state-of-the-art polymer-based electrolytes. The Li|Li symmetric cells assembled with FNCDs-SPE demonstrate stable cycling for over 2000 hours. Full cells incorporating FNCDs-SPE paired with commercial cathodes including LiFePO₄ (LFP), LiCoO₂ (LCO), and LiNi_{0.8}Co_{0.1}Mn_{0.1}O₂ (NCM811) all demonstrate outstanding capacity retention and rate capability. This study provides valuable insights into the design of high-performance SPEs through functional nanofiller engineering and paves a way toward practical high-safety and high-energy-density solid-state batteries.

2 Experimental

2.1 Synthesis of NCDs and FNCDs

Nitrogen-doped carbon quantum dots (NCDs) were synthesized via a solvothermal method. Specifically, 1 g of anhydrous citric acid and 0.8 g of m-phenylenediamine were dissolved in 10 mL of formamide under magnetic stirring until a homogeneous solution was obtained. The mixture was then transferred to a Teflon-lined stainless-steel autoclave and heated at 160 °C for 4 h. After the autoclave had cooled to room temperature, the resulting brownish-black solution was mixed with 30 mL of ethanol. The mixture was then centrifuged, and the precipitate was collected and washed with ethanol several times to remove impurities. This washing cycle was repeated three times. The purified precipitate was re-dispersed in deionized water, dialyzed against fresh deionized water for 36 h, and finally lyophilized to yield the NCDs as a solid powder.

FNCDs were obtained via a one-step fluorination of the as-synthesized NCDs. Typically, 250 mg of NCDs were dispersed in 19 mL of ethanol by ultrasonication for 30 min. The dispersion was then transferred to a Teflon-lined autoclave, followed by the addition of 1 mL of a 40 wt% hydrofluoric acid (HF) aqueous solution. The autoclave was sealed and maintained at 160 °C for 12 h to facilitate the fluorination reaction. After cooling to room temperature, the crude product was transferred to a Teflon beaker. To neutralize any residual HF, 25 mL of a saturated sodium bicarbonate (NaHCO₃) aqueous solution was added slowly, followed by the addition of 100 mL of deionized water. The mixture was then centrifuged, and the collected solid was washed repeatedly with deionized water until the supernatant reached neutral pH. The final product (FNCDs) was obtained by lyophilization.

2.2 Preparation of FNCDs-based electrolyte films

The FNCDs-SPE films were fabricated using a solution casting technique. First, 1 g of PVDF-HFP (average Mw = ~600,000) and 1 g of bis(trifluoromethanesulfonyl)imide lithium salt (LiTFSI) were dissolved in 7 mL of N, N-dimethylformamide (DMF) in a glass vial under magnetic stirring at 80 °C for 20 min. Subsequently, a predetermined amount of the ionic liquid plasticizer 1-Allyl-2,3-dimethylimidazolium chloride (AmimCl) and 50 mg of FNCDs powder were added to the above solution. The mixture was continuously stirred at 80 °C for 12 h to obtain a homogeneous and viscous casting solution. The casting solution was then poured onto a leveled polytetrafluoroethylene (PTFE) dish and allowed to rest for initial solvent evaporation. The dish was then transferred to a vacuum oven and dried at 80 °C for 24 h to thoroughly remove the DMF solvent, yielding a freestanding FNCDs-SPE film. The film was finally cut into disks of desired dimensions for subsequent measurements and cell assembly. For comparison, control electrolyte films, denoted as NCDs-SPE and P-SPE (pristine SPE), were prepared following the identical procedure but by replacing the 50 mg of FNCDs with an equal mass of NCDs or by omitting the carbon quantum dot filler entirely, respectively.

2.3 Materials characterization and electrochemical measurements

The morphology, chemical structure, and physicochemical properties of the synthesized carbon quantum dots (NCDs, FNCDs) and the solid polymer electrolyte films were thoroughly investigated. The electrochemical performance, including ionic conductivity, lithium-ion transference number, electrochemical stability window, and cycling stability in both symmetric Li|Li



cells and full cells (with LFP, LCO, and NCM811 cathodes), was systematically evaluated. Detailed descriptions of the characterization techniques, measurement procedures, and specific instrument parameters are provided in the Supporting Information.

3 Results and discussion

NCDs and FNCDs are synthesized through a simple hydrothermal process. Constant high temperature provides a favorable environment for the carbonization, polymerization and cross-linking of citric acid (CA) and *m*-phenylenediamine (*m*-PD), leading to the formation of zero-dimensional carbon nanomaterials. The surface of NCDs is rich in C=O and -OH functional groups, which provides active sites for subsequent fluorination (Fig. S1). The formation of C-F bonds occurs via insertion of HF into defect sites of NCDs, forming reactive intermediates that subsequently undergo addition to C=C bonds or substitution with oxygen-containing groups, yielding covalently bonded fluorine on the carbon dot surface.²⁶ As illustrated in Fig. 1a, the solid polymer electrolyte is fabricated using a solution casting method. The FNCDs are incorporated into the PVDF-HFP matrix, where they act as cross-linking sites and are uniformly dispersed among the polymer chains. This uniform dispersion effectively suppresses polymer crystallization, thereby enhancing the mechanical strength and toughness of the electrolyte. Meanwhile, an ionic liquid (IL) is introduced as a plasticizer.¹⁷ After solvent evaporation, a light-yellow, flexible freestanding film, denoted as FNCDs-SPE, is obtained.

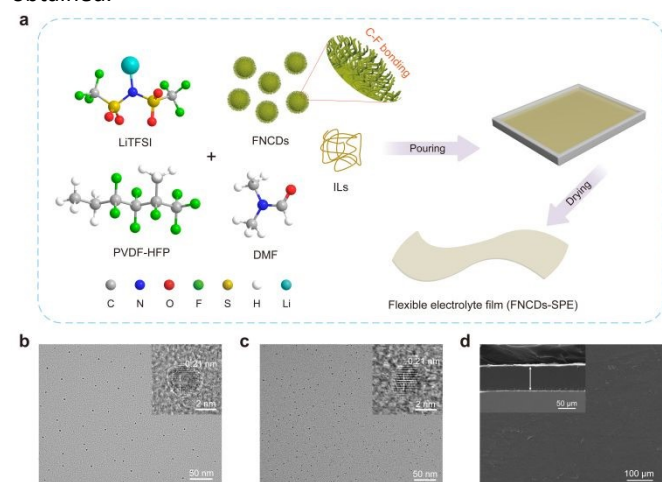


Fig. 1 (a) Schematic illustration of the synthetic route of FNCDs-SPE. TEM images of (b) NCDs and (c) FNCDs. (d) SEM image of FNCDs-SPE film. The insets of (b) and (c) are HRTEM images of NCDs and FNCDs, respectively. The inset of (d) is the cross-sectional SEM image of FNCDs-SPE film.

The morphologies and structures of NCDs and FNCDs were investigated by transmission electron microscopy (TEM). The TEM images (Fig. 1b and 1c) reveal that both NCDs and FNCDs are uniformly dispersed and exhibit a quasi-spherical morphology. Statistical analysis of over 100 nanoparticles (Fig.

S2) indicates that both samples have a similar average particle size of approximately 2.5 nm. The lattice fringe spacings measured from high-resolution TEM (HRTEM) images (insets of Fig. 1b and 1c) are ~ 0.21 nm, corresponding to the (100) plane of graphite.²⁷ The morphology of the polymer electrolyte film was examined by scanning electron microscopy (SEM). As shown in Fig. 1d, the surface of the FNCDs-SPE film is smooth and dense without visible cracks or pores, which is further confirmed by its cross-sectional view (inset of Fig. 1d). The thickness of the electrolyte film is approximately 67 μm . In contrast, the surfaces of the control NCDs-SPE and P-SPE films are comparatively rough (Fig. S3). Their cross-sectional images reveal the presence of some pores and inhomogeneous regions, which could result in uneven Li^+ flux and localized high current density, ultimately impairing battery performance. The dense and homogeneous structure of FNCDs-SPE is conducive to rapid and uniform Li^+ transport. This improved uniformity is attributed to the strong interactions, such as hydrogen bonding, between the FNCDs and the polymer chains.

The surface chemical structures of NCDs and FNCDs were characterized by Fourier transform infrared spectroscopy (FT-IR), nuclear magnetic resonance (NMR) spectroscopy and X-ray photoelectron spectroscopy (XPS). The FT-IR spectra (Fig. 2a) display several broad absorption bands from 500 to 4000 cm^{-1} . The peaks at 3442 and 1627 cm^{-1} correspond to the stretching vibrations of O-H and C=O bonds, respectively. Notably, a distinct absorption peak at 1209 cm^{-1} appears in the spectrum of FNCDs, which is assigned to the C-F stretching vibration.²⁸ On the contrary, this peak is absent in the spectrum of NCDs, confirming the successful introduction of fluorine atoms onto the carbon dot surface. To further investigate the chemical state of fluorine in FNCDs, we performed solid-state ^{19}F NMR analysis on the FNCDs sample. The ^{19}F NMR spectrum (Fig. S4) exhibits main signals in the range of -140 to -170 ppm, characteristic of covalent C-F bonds such as $\text{C}(\text{sp}^3)\text{-F}$ and $\text{C}(\text{sp}^2)\text{-F}$ bonds.²⁹ No detectable signal is observed at around -224 ppm (characteristic of ionic fluoride, e.g., NaF),³⁰ confirming the absence of residual fluoride salts. These results confirm that fluorine in FNCDs exists primarily as C-F bonds. Furthermore, XPS analysis was employed to probe the surface composition and bonding states. The XPS survey spectrum (Fig. 2b) confirms that FNCDs are composed of C, N, O, and F. The absence of F 1s peak in the survey spectrum of NCDs is consistent with the FT-IR results. The high-resolution F 1s XPS spectrum of FNCDs (Fig. 2c) shows two peaks at 684.3 and 686.3 eV, corresponding to $\text{C}(\text{sp}^2)\text{-F}$ and $\text{C}(\text{sp}^3)\text{-F}$ bonds, respectively.²⁸



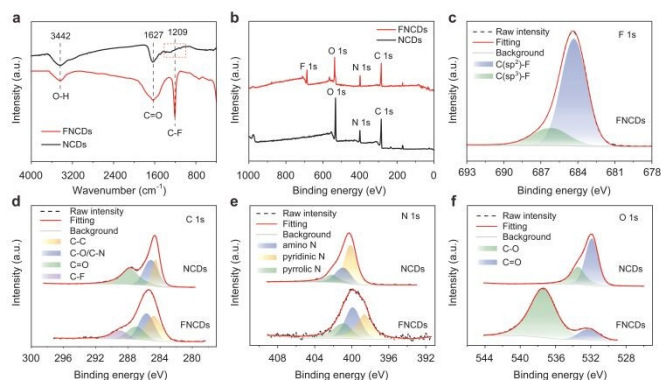


Fig. 2 (a) FT-IR spectra and (b) XPS survey spectra of NCDs and FNCDs. (c) High-resolution F 1s XPS spectrum of FNCDs. High-resolution (d) C 1s, (e) N 1s and (f) O 1s XPS spectra of NCDs and FNCDs.

The integrated areas of the F 1s XPS peaks indicate that the contents of C(sp³)-F bonds and C(sp²)-F bonds are 21.84% and 78.16%, respectively. The C(sp³)-F bonds primarily originate from the fluorination substitution of oxygen-containing functional groups (such as -OH and -COOH) located at the edges and defect sites of the carbon dots, which are the most chemically active regions on the carbon dot surface.³¹ Their strong electron-withdrawing effect can more effectively decouple Li⁺-TFSI⁻ interactions and promote lithium salt dissociation. The C(sp²)-F bonds are mainly situated within the carbon skeleton plane and contribute to modulating the electronic structure and stability of the carbon dots.³²

Deconvolution of the high-resolution C 1s spectrum of NCDs (Fig. 2d) reveals peaks at 284.8, 285.4 and 288.0 eV, attributable to C-C, C-O/C-N and C=O bonds, respectively. In contrast, the C 1s spectrum of FNCDs shows an additional distinct peak at 289.1 eV, which is assigned to the C-F bond.²³ The high-resolution N 1s spectra (Fig. 2e) indicate that nitrogen in both NCDs and FNCDs exists primarily in the forms of amino N (400.9 and 399.9 eV), pyridinic N (400.2 and 398.6 eV) and pyrrolic N (402.1 and 401.0 eV). The high-resolution O 1s spectra (Fig. 2f) are deconvoluted into two components, corresponding to C=O and C-O bonds. For NCDs, these peaks are located at 531.9 and 533.45 eV, respectively. After fluorination, the respective binding energies for FNCDs shift to 532.3 and 537.4 eV.³³ Following fluorination, the intensity of the C=O component decreases significantly, while the C-O component increases and shifts to a higher binding energy. This suggests the presence of multiple types of C-F bonds including C(sp²)-F and C(sp³)-F on the carbon dot skeleton. The notable increase in binding energy is attributed to the strong electron-withdrawing inductive effect of fluorine atoms, which reduces the electron cloud density around both the carbon and oxygen atoms.

The crystallinity and component interactions within the FNCDs-SPE film were investigated by X-ray diffraction (XRD). As shown in Fig. 3a, the characteristic diffraction peaks belonging to FNCDs and LiTFSI are absent in the XRD pattern of FNCDs-SPE, indicating the formation of a predominantly amorphous structure. Furthermore, the diffraction peak of pure PVDF-HFP at 18.2° disappears in the FNCDs-SPE pattern. This can be

ascribed to the incorporated FNCDs disrupting the conformational rearrangement and packing of the polymer chains, thereby significantly reducing its crystallinity. A comparison of the XRD patterns for FNCDs-SPE, NCDs-SPE, and P-SPE films (Fig. S5) further confirms that FNCDs are most effective in promoting amorphization of the polymer matrix, which is favorable for segmental motion and Li⁺ transport. Correspondingly, the FNCDs-SPE film exhibits excellent flexibility and mechanical strength (Fig. S6), which are crucial for suppressing lithium dendrite penetration. Quantitative tensile tests (Fig. S7 and Table S1) reveal that the FNCDs-SPE film possesses the highest elongation at break (249.2%). Although its tensile strength (3.54 MPa) is lower than that of NCDs-SPE (5.77 MPa), it remains substantially higher than that of the P-SPE (1.58 MPa), demonstrating a good balance between toughness and strength. The thermal stability of these three electrolyte films was examined by thermogravimetric analysis (TGA). TGA curves (Fig. S8) show that all electrolyte films exhibit comparable thermal stability, undergoing a two-stage weight loss corresponding to residual solvent evaporation followed by decomposition of the lithium salt and polymer.²¹

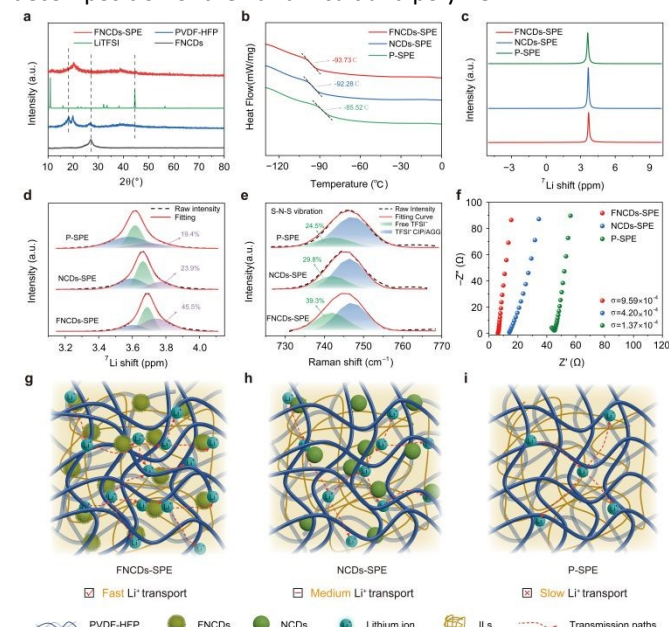


Fig. 3 (a) XRD patterns of FNCDs-SPE film and the related components. (b) DSC curves, (c) ⁷Li solid-state NMR spectra, (d) the corresponding fitting peaks in the ⁷Li NMR spectra and (e) Raman spectra of FNCDs-SPE, NCDs-SPE and P-SPE films. (f) Nyquist plots in stainless steel (SS) symmetric cells of FNCDs-SPE, NCDs-SPE and P-SPE. (g) Schematic illustrations of possible Li⁺ transmission paths in FNCDs-SPE, (h) NCDs-SPE and (i) P-SPE.

Differential scanning calorimetry (DSC) results (Fig. 3b) show that the FNCDs-SPE film has the lowest glass transition temperature ($T_g = -93.73$ °C) compared to NCDs-SPE (-92.28 °C) and P-SPE (-85.52 °C), confirming enhanced chain mobility, which facilitates Li⁺ transport.^{34,35} To investigate the local lithium chemical environments, solid-state ⁷Li NMR spectroscopy was performed. Compared with P-SPE, the ⁷Li NMR signal of carbon dot-filled SPEs shifts to higher field (Fig.



3c), indicating a weaker interaction between Li^+ and the PVDF-HFP matrix after filling NCDs or FNCDs. By fitting the ^7Li NMR spectra, distinct Li^+ environments are identified (Fig. 3d). The peak at higher field (shaded in purple) is typically associated with mobile Li^+ , which contributes more effectively to ionic conduction. This mobile Li^+ fraction accounts for 45.5% in FNCDs-SPE, significantly higher than that in NCDs-SPE (23.9%) and P-SPE (19.4%). In contrast, the lower-field components correspond to Li^+ trapped by oxygen or fluorine in PVDF-HFP, which are less conducive to migration.³⁶ These results confirm that FNCDs facilitate the release of mobile Li^+ . Raman spectroscopy was employed to probe the change of the Li-TFSI interaction within the polymer electrolytes (Fig. 3e). The characteristic band near 745 cm^{-1} , associated with the S-N-S deformation of the TFSI⁻ anion, is deconvoluted to quantify the populations of free TFSI⁻ (741.6 cm^{-1}), contact ion pairs (CIPs), and ion aggregates (AGGs).^{37,38} The FNCDs-SPE film shows the highest proportion of free TFSI⁻ (39.3%), indicating the most effective promotion of LiTFSI dissociation. This suggests that more Li^+ ions are liberated to coordinate with and migrate along the FNCDs and polymer chains, resulting in higher ionic conductivity. In contrast, a higher proportion of Li^+ in the NCDs-SPE and P-SPE films exists as CIPs or AGGs, which impedes cationic mobility. This analysis is also supported by FT-IR spectra (Fig. S9), where the S=O stretching vibration of TFSI⁻ shifts to lower wavenumbers in the composites, signifying changes in its chemical environment.¹⁷

Electrochemical impedance spectroscopy (EIS) reveals that the FNCDs-SPE electrolyte has the lowest bulk resistance (Fig. 3f), leading to the highest ionic conductivity of $9.59 \times 10^{-4}\text{ S cm}^{-1}$, as calculated from Table S2 and equation (1) in supporting information. This value is significantly higher than those of NCDs-SPE ($4.20 \times 10^{-4}\text{ S cm}^{-1}$) and P-SPE ($1.37 \times 10^{-4}\text{ S cm}^{-1}$). A schematic illustration of the proposed Li^+ transport mechanisms in the three electrolytes is presented in Fig. 3g-i. The superior conductivity of FNCDs-SPE originates from two synergistic effects. First, the uniformly dispersed FNCDs act as physical cross-linkers, disrupting polymer chain order and expanding the amorphous domain for faster segmental motion. Second, the abundant surface functional groups (e.g., C-F, C-N, -OH, -COOH) on FNCDs engage in Lewis acid-base interactions with Li^+ , providing numerous additional hopping sites for ion transport. Specifically, the fluorine atoms with strong electron-withdrawing effect weaken the coupling between Li^+ and TFSI⁻, thereby promoting salt dissociation,³⁹ while the nitrogen-containing groups enhance the lithophilicity of the filler, reducing the nucleation overpotential for Li^+ deposition.⁴⁰ These combined effects establish continuous and efficient conduction pathways, leading to the observed enhancement in ionic conductivity and Li^+ transference number.

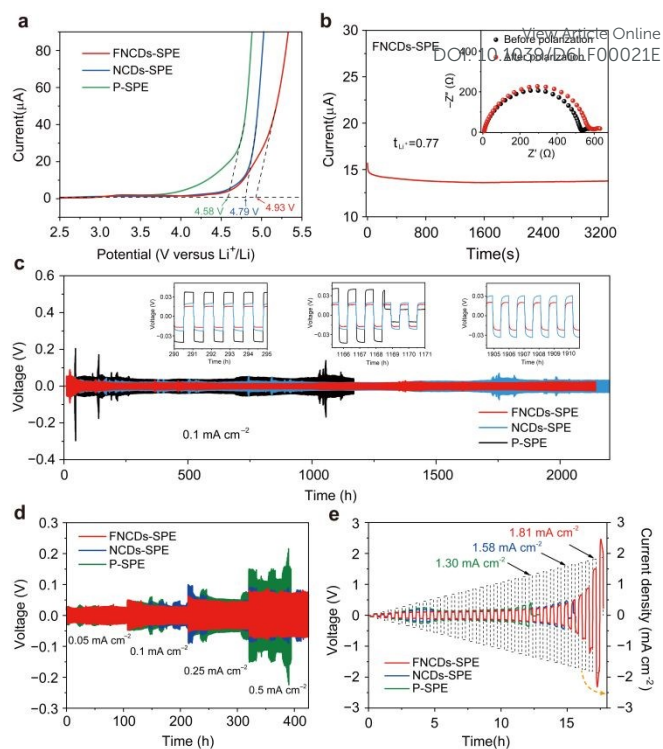


Fig. 4 (a) LSV curves in Li||Li symmetrical cells of FNCDs-SPE, NCDs-SPE and P-SPE. (b) Polarization curves of Li||FNCDs-SPE||Li cell (inset: the impedance diagram before and after polarization). (c) Galvanostatic cycling curves in Li||Li symmetrical cells of FNCDs-SPE, NCDs-SPE and P-SPE at current density of 0.1 mA cm^{-2} (inset: local magnification curves). (d) The cycling curves in Li||Li symmetrical cells of FNCDs-SPE, NCDs-SPE and P-SPE at different current densities. (e) Critical current density (CCD) curves in Li||Li symmetrical cells of FNCDs-SPE, NCDs-SPE and P-SPE.

The electrochemical performance of the electrolytes was further investigated using Li||Li symmetric cells. Linear sweep voltammetry (LSV) results (Fig. 4a) demonstrate that the FNCDs-SPE electrolyte possesses the widest electrochemical stability window (up to 4.93 V vs. Li/Li^+), compared to NCDs-SPE (4.79 V) and P-SPE (4.58 V), indicating its compatibility with high-voltage cathodes. The chronoamperometry tests (Fig. 4b) show that the FNCDs-SPE electrolyte also achieves the highest Li^+ transference number ($t_{\text{Li}^+} = 0.77$), confirming that ionic conduction is predominantly cationic.⁴¹ In contrast, the NCDs-SPE and P-SPE electrolytes exhibit lower t_{Li^+} values of 0.66 and 0.41, respectively (Fig. S10 and Table S3). Galvanostatic cycling tests (Fig. 4c) of these three cells at a current density of 0.1 mA cm^{-2} demonstrate stable cycling for over 2000 h. The Li||FNCDs-SPE||Li cell exhibits the lowest polarization voltage ($\sim 20\text{ mV}$) and the most stable long-term performance, indicating uniform lithium deposition and stripping behavior. By contrast, the Li||P-SPE||Li cell shows inferior cycling stability, experiencing a premature short circuit after 1,168 h, which is likely attributable to lithium dendrite penetration through the electrolyte film. Even when the current density is increased from 0.05 to 0.5 mA cm^{-2} , the Li||FNCDs-SPE||Li cell maintains stable cycling with a



relatively low polarization voltage (Fig. 4d). This enhanced stability is ascribed to the abundant functional groups on the FNCDs, which help homogenize the Li^+ flux at the electrode interface, thereby guiding uniform lithium deposition/stripping and suppressing dendrite growth. The critical current density (CCD), which defines the maximum sustainable current before cell failure, was also evaluated.^{42,43} As shown in Fig. 4e, the CCD value of the $\text{Li}||\text{FNCDs-SPE}||\text{Li}$ cell (1.81 mA cm^{-2}) is significantly higher than those of the $\text{Li}||\text{NCDs-SPE}||\text{Li}$ (1.58 mA cm^{-2}) and $\text{Li}||\text{P-SPE}||\text{Li}$ cells (1.30 mA cm^{-2}), highlighting the beneficial role of the functional fillers.

To gain deeper insights into the superior cycling stability of the FNCDs-SPE-based cells, the electrode/electrolyte interface was systematically investigated using a combination of electrochemical and post-mortem analyses. First, electrochemical impedance spectroscopy (EIS) was performed on the cycled $\text{Li}||\text{Li}$ symmetric cells, and the data were deconvoluted using the distribution of relaxation times (DRT) method to decouple the various interfacial contributions. As shown in Fig. 5a, the $\text{Li}||\text{FNCDs-SPE}||\text{Li}$ cell exhibits the smallest overall impedance (413Ω). The corresponding DRT spectra (Fig. 5b) effectively separate the frequency-dependent processes: the time constant (τ) at around 10^{-5} s corresponds to the ohmic resistance (R_b) from the electrolyte and electrode components; processes with τ ranging from 10^{-4} to 10^{-2} s are attributed to the SEI layer resistance (R_{SEI}); and the τ range of 10^{-5} to 10^1 s corresponds to the charge transfer resistance (R_{ct}).^{44,45} Throughout the entire spectrum, the FNCDs-SPE electrolyte consistently exhibits the lowest values for both R_{SEI} and R_{ct} , indicating more stable interfacial reaction kinetics and suppressed side reactions during cycling.⁴⁶ This enhanced interfacial stability is directly reflected in the lithium deposition morphology. Post-mortem SEM images (Fig. 5c,d) after 100 cycles at 0.25 mA cm^{-2} reveal a significantly smoother and more uniform lithium metal surface in the $\text{Li}||\text{FNCDs-SPE}||\text{Li}$ cell compared to the rough, dendritic surface observed in the $\text{Li}||\text{P-SPE}||\text{Li}$ cell, providing direct visual evidence of effective dendrite suppression.⁴⁷ To further understand the origin of this uniform deposition, XPS depth profiling was conducted on the cycled lithium electrodes to probe the chemical composition and thickness of the SEI layer. As shown in Fig. 5e,f and Fig. S11, the F 1s spectra reveal the presence of C–F bonds and LiF, which are typical decomposition products originating from the PVDF-HFP matrix and LiTFSI salt.⁴⁸ Notably, when FNCDs-SPE is used, the intensities of these decomposition components are consistently lower throughout the depth profile compared to those observed with P-SPE. This indicates that parasitic reactions between the electrolyte and lithium metal are significantly mitigated with the incorporation of FNCDs. The Li 1s spectra (Fig. 5g,h) further corroborate this finding: after 700 s of sputtering, a distinct Li metal signal at 54.5 eV appears for the $\text{Li}||\text{FNCDs-SPE}||\text{Li}$ cell, whereas no such signal is detected for the $\text{Li}||\text{P-SPE}||\text{Li}$ cell. This confirms the formation of a thinner SEI layer when FNCDs-SPE is employed, which is beneficial for rapid Li^+ transport and reduced interfacial resistance.⁴⁹ Additionally, the O 1s and S 2p spectra (Fig. S12) show lower contents of Li_2CO_3 , residual LiTFSI, and Li_2S in the FNCDs-SPE case, suggesting suppressed oxidative decomposition at the interface and the formation of a more uniform and robust SEI layer.²¹ These combined results demonstrate that the FNCDs filler not only facilitates rapid ion

conduction but also plays a critical role in constructing a stable and thin SEI, which collectively contribute to the exceptional cycling stability of the FNCDs-SPE-based cells.

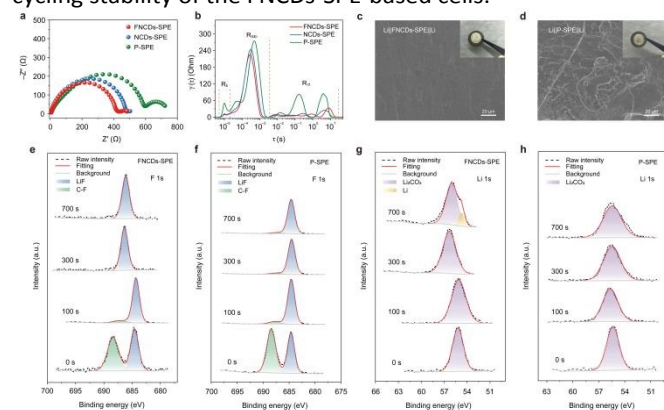


Fig. 5 (a) Nyquist plots of $\text{Li}||\text{Li}$ symmetric cells with FNCDs-SPE, NCDs-SPE, and P-SPE after 100 cycles and (b) corresponding DRT analysis of the EIS spectra. SEM images of the lithium metal surface after 100 cycles in (c) $\text{Li}||\text{FNCDs-SPE}||\text{Li}$ cell and (d) $\text{Li}||\text{P-SPE}||\text{Li}$ cell. XPS depth profiles of the F 1s and Li 1s spectra for (e,g) FNCDs-SPE and (f,h) P-SPE.

Full cells with lithium metal anode and commercial cathodes were assembled to further evaluate the overall performance of the electrolyte films. The charge/discharge profiles of the $\text{LFP}||\text{FNCDs-SPE}||\text{Li}$ cell (Fig. 6a) show a reversible specific capacity of 153.9 mAh g^{-1} at 0.1 C , which is higher than those of the $\text{LFP}||\text{NCDs-SPE}||\text{Li}$ (145.2 mAh g^{-1}) and $\text{LFP}||\text{P-SPE}||\text{Li}$ cells (131.3 mAh g^{-1}) (Fig. S13). At a higher rate of 2 C , the $\text{LFP}||\text{FNCDs-SPE}||\text{Li}$ cell exhibits the smallest capacity decay, retaining a capacity of 115.6 mAh g^{-1} . The rate performance of the $\text{LFP}||\text{FNCDs-SPE}||\text{Li}$ cell is shown in Fig. 6b. It delivers specific capacities of 153.9 , 151.0 , 145.8 , 135.9 , and 115.6 mAh g^{-1} at 0.1 , 0.2 , 0.5 , 1 , and 2 C , respectively. Notably, when the rate is switched back to 0.1 C , the $\text{LFP}||\text{FNCDs-SPE}||\text{Li}$ cell demonstrates better capacity recovery compared to the $\text{LFP}||\text{NCDs-SPE}||\text{Li}$ and $\text{LFP}||\text{P-SPE}||\text{Li}$ cells. The cycling performance at 0.1 C is shown in Fig. 6c. After 100 cycles, the $\text{LFP}||\text{FNCDs-SPE}||\text{Li}$ cell maintains a discharging capacity of 142.8 mAh g^{-1} and a capacity retention of 95.6% , superior to that of the $\text{LFP}||\text{NCDs-SPE}||\text{Li}$ cell (123.4 mAh g^{-1} and 87.7%). The capacity of the $\text{LFP}||\text{P-SPE}||\text{Li}$ cell dropped sharply after 80 cycles, indicating issues related to uneven lithium deposition/stripping. When cycled at a higher rate of 1 C (Fig. 6d), the $\text{LFP}||\text{FNCDs-SPE}||\text{Li}$ cell demonstrates excellent long-term stability, retaining 81.8% of its initial capacity after 500 cycles. In contrast, the capacities of the $\text{LFP}||\text{NCDs-SPE}||\text{Li}$ and $\text{LFP}||\text{P-SPE}||\text{Li}$ cells decline rapidly, indicating the outstanding interfacial stability of the FNCDs-SPE-based cell. The corresponding charge/discharge voltage profiles of the $\text{LFP}||\text{FNCDs-SPE}||\text{Li}$ cell at different cycles are shown in Fig. 6e. Even with a higher active material loading of 6.09 mg cm^{-2} (Fig. 6f), the $\text{LFP}||\text{FNCDs-SPE}||\text{Li}$ cell exhibits a discharging capacity of 126.8 mAh g^{-1} and a capacity retention of 86.8% after 100 cycles at 0.1 C , demonstrating the practical robustness of the FNCDs-SPE electrolyte.



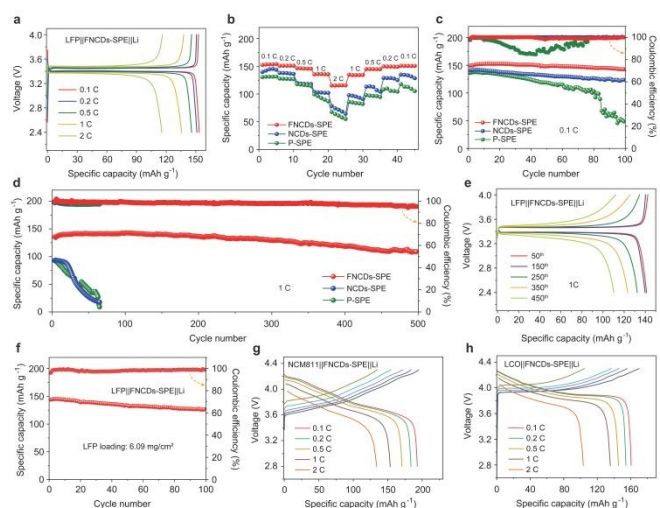


Fig. 6 (a) The charge/discharge curves of LFP||FNCDs-SPE||Li cell at different current densities. (b) The rate performance at 0.1-2 C and (c) cycling performance at 0.1 C of LFP||FNCDs-SPE||Li, LFP||NCDs-SPE||Li and LFP||P-SPE||Li cells. (d) The long-term cycling performance of LFP||FNCDs-SPE||Li, LFP||NCDs-SPE||Li and LFP||P-SPE||Li cells at 1 C. (e) The charge/discharge curves of LFP||FNCDs-SPE||Li cell at 1 C. (f) The cycling performance of LFP||FNCDs-SPE||Li cell under LFP loading of 6.09 mg cm⁻² at 0.1 C. The charge/discharge curves of (g) NCM811||FNCDs-SPE||Li cell and (h) LCO||FNCDs-SPE||Li at different rates.

To assess broader compatibility, the FNCDs-SPE was paired with other commercial high-voltage cathodes, such as NCM811 and LCO. As shown in Fig. 6g, the NCM811||FNCDs-SPE||Li cell delivers high reversible specific capacities of 192.9 mAh g⁻¹ at 0.1 C and 134.0 mAh g⁻¹ at 2 C, both substantially higher than those of the NCM811||NCDs-SPE||Li (171.6 and 90.7 mAh g⁻¹) and NCM811||P-SPE||Li cells (142.1 and 85.8 mAh g⁻¹) (Fig. S14). The NCM811||FNCDs-SPE||Li cell also shows the best cycling stability and rate performance among the three electrolytes (Fig. S15), attributable to the key role of FNCDs in facilitating ion transport and stabilizing the interface. Similarly, the LCO||FNCDs-SPE||Li cell (Fig. 6h) demonstrates superior cycling and rate performance compared to the LCO||NCDs-SPE||Li and LCO||P-SPE||Li cells (Fig. S16,17). It is noteworthy that the LCO cathode itself exhibits inferior cycling stability and rate capability retention compared to both NCM811 and LFP, which is inherently linked to the structural and chemical instability of LCO at high operating voltages. Compared with other recently reported polymer electrolytes, our FNCDs-SPE film shows competitive advantages in overall performance (Table S4).

These findings collectively demonstrate that the FNCDs-SPE electrolyte, with its rapid Li⁺ conduction, robust mechanical properties, and excellent compatibility with various commercial cathodes, presents a promising strategy for developing high-performance, safe, and reliable solid-state batteries for practical applications.

Conclusions

View Article Online
DOI: 10.1039/D6LF00021E

In summary, we develop fluorine-nitrogen modified carbon dots (FNCDs) and incorporated them as functional fillers to fabricate a flexible solid polymer electrolyte (FNCDs-SPE) for high-rate lithium-ion conduction. The ~2.5 nm FNCDs are uniformly dispersed within the PVDF-HFP matrix. Their abundant fluorine- and oxygen-containing surface functional groups interact with the polymer chains, effectively disrupting the chain packing and crystallinity, thereby increasing the amorphous phase content. This structural modification, coupled with the Lewis acid-base interactions between the FNCDs and Li⁺ that provide additional hopping sites, collectively leads to a significant enhancement in ionic conductivity. The resulting rapid and uniform ion transport promotes stable lithium deposition/stripping and improves the interfacial stability. Consequently, the FNCDs-SPE outperforms both the NCDs-SPE and P-SPE in long-term cycling and rate capability. Furthermore, the FNCDs-SPE demonstrates excellent compatibility with various high-voltage commercial cathodes (LFP, LCO, NCM811), highlighting its great promise for practical applications. This work provides a valuable strategy for the design of high-performance, safe, and reliable solid-state battery electrolytes through functional nanofiller engineering.

Author contributions

Yang Wu: investigation, experiment, writing original draft, data curation. Wenbo Yue: writing review and editing, supervision, project administration, conceptualization.

Conflicts of interest

There are no conflicts to declare.

Data availability

The data supporting this article have been included as part of the ESI. The data that support the findings of this study are available from the corresponding author upon reasonable request.

Acknowledgements

This work was financially supported by the Beijing Natural Science Foundation (Z240025).

Notes and references

- H. Xie, J. Feng, H. Zhao, *Energy Storage Mater.*, 2023, **61**, 102918.
- Z. Zhang, W. Han, *Nano-Micro Lett.*, 2024, **16**, 24.
- X. Yang, Y. Wang, Y. Guo, Z. Liao, W. Fu, J. Liu, *J. Mater. Chem. A*, 2024, **12**, 14848–14865.
- X. Xie, P. Zhang, X. Li, Z. Wang, X. Qin, M. Shao, L. Zhang, W. Zhou, *J. Am. Chem. Soc.*, 2024, **146**, 5940-5951.



- 5 T. Schmaltz, F. Hartmann, T. Wicke, L. Weymann, C. Neef, J. Janek, *Adv. Energy Mater.*, 2023, **13**, 2301886.
- 6 H. Guo, R. Shu, X. Xie, X. Wang, H. Wu, Y. Song, J. Tian, F. Cheng, Y. Guo, T. Zhu, L. Shi, R. Wen, Q. Yi, *J. Mater. Chem. A*, 2025, **13**, 25998–26008.
- 7 T. Famprakis, P. Canepa, J. A. Dawson, M. S. Islam, C. Masquelier, *Nat. Mater.*, 2019, **18**, 1278–1291.
- 8 Y. Chen, J. Qian, K. Wang, L. Li, F. Wu, R. Chen, *Adv. Mater.*, 2025, **37**, 2502653.
- 9 Y. Xu, X. Xiong, J. Peng, Q. Zhou, W. Wu, W. Gao, Y. Peng, T. Wang, F. Wang, Y. Wu, *J. Mater. Chem. A*, 2024, **12**, 26848–26856.
- 10 A. Banerjee, X. Wang, C. Fang, E. Wu, Y. Meng, *Chem. Rev.*, 2020, **120**, 6878–6933.
- 11 X. Zhang, S. Cheng, C. Fu, G. Yin, L. Wang, Y. Wu, H. Huo, *Nano-Micro Lett.*, 2025, **17**, 2.
- 12 Q. Kang, Z. Zhuang, Y. Liu, Z. Liu, Y. Li, B. Sun, F. Pei, H. Zhu, H. Li, P. Li, Y. Lin, K. Shi, Y. Zhu, J. Chen, C. Shi, Y. Zhao, P. Jiang, Y. Xia, D. Wang, X. *Adv. Mater.*, 2023, **35**, 2303460.
- 13 S. Wang, S. Xiao, S. Li, C. Liu, H. Cai, W. Sun, Z. Huang, W. Lai, *Angew. Chem. Int. Ed.*, 2024, **63**, e202412434.
- 14 K. Wu, A. Li, J. Tan, F. Zhou, H. Yan, P. Wang, T. Xie, Q. Zeng, C. Han, Q. Liu, B. Li, *Angew. Chem. Int. Ed.*, 2024, **63**, e202410347.
- 15 H. Liang, L. Wang, A. Wang, Y. Song, Y. Wu, Y. Yang, X. He, *Nano-Micro Lett.*, 2023, **15**, 42.
- 16 Q. Wang, H. Zhang, Z. Cui, Q. Zhou, X. Shangguan, S. Tian, X. Zhou, G. Cui, *Energy Storage Mater.*, 2019, **23**, 466–490.
- 17 J. Li, Z. Hu, S. Zhang, H. Zhang, S. Guo, G. Zhong, Y. Qiao, Z. Peng, Y. Li, S. Chen, G. Chen, A. Cao, *Nat. Sustain.*, 2024, **7**, 1481–1491.
- 18 M. Nguyen, H. Nguyen, T. Duong, S. Kim, J. Kim, J. Bae, H. Kim, S. Lim, W. Ahn, *Adv. Funct. Mater.*, 2024, **34**, 2406987.
- 19 X. Zhang, M. Nitou, W. Li, Z. Wan, L. Liu, Z. Luo, S. Muhammad, W. Qin, L. An, Y. Niu, W. Lv, *Chin. Chem. Lett.*, 2023, **34**, 108245.
- 20 X. He, Y. Ni, Y. Hou, Y. Lu, S. Jin, H. Li, Z. Yan, K. Zhang, J. Chen, *Angew. Chem. Int. Ed.*, 2021, **60**, 22672–22677.
- 21 G. Feng, Q. Ma, D. Luo, T. Yang, Y. Nie, Z. Zheng, L. Yang, S. Li, Q. Li, M. Jin, X. Wang, Z. Chen, *Angew. Chem. Int. Ed.*, 2025, **64**, e202413306.
- 22 S. Sikiru, T. Oladosu, S. Kolawole, L. Mubarak, H. Soleimani, L. Afolabi, A. Toyin, *J. Energy Storage*, 2023, **60**, 106556.
- 23 L. Xu, S. Li, H. Tu, F. Zhu, H. Liu, W. Deng, J. Hu, G. Zou, H. Hou, X. Ji, *ACS Nano*, 2023, **17**, 22082–22094.
- 24 C. Ma, K. Dai, H. Hou, X. Ji, L. Chen, D. Ivey, W. Wei, *Adv. Sci.*, 2018, **5**, 1700996.
- 25 J. Ni, X. Zhang, T. Song, Z. Huang, Q. Ma, T. He, H. Xiong, *Chem. Eng. J.*, 2024, **500**, 157379.
- 26 Y. Sato, T. Kume, R. Hagiwara, Y. Ito, *Carbon*, 2003, **41**, 351–357.
- 27 H. Shi, Y. Wu, J. Xu, C. Zhou, H. Xu, W. Ye, Y. Yin, Z. Wang, R. Su, Z. An, H. Shi, *Chem. Eng. J.*, 2023, **476**, 146524.
- 28 P. Long, Y. Feng, Y. Li, C. Cao, S. Li, H. An, C. Qin, J. Han, W. Feng, *ACS Appl. Mater. Interfaces*, 2017, **9**, 37981–37990.
- 29 M. Murakami, K. Matsumoto, R. Hagiwara, Y. Matsuo, *Carbon*, 2018, **138**, 179–187.
- 30 M. Lowe, B. Gallant, N. Davison, M. Hopkinson, D. Kubicki, E. Lu, R. Armstrong, *J. Am. Chem. Soc.*, 2025, **147**, 40895–40899.
- 31 Q. Yang, Z. Chi, Q. Li, S. Scheiner, *J. Chem. Phys.*, 2020, **153**, 074304.
- 32 P. Panini, R. Gonnade, D. Chopra, *New J. Chem.*, 2016, **40**, 4981–5001.
- 33 F. Zhu, L. Xu, X. Hu, M. Yang, H. Liu, C. Gan, W. Deng, G. Zou, H. Hou, X. Ji, *Angew. Chem. Int. Ed.*, 2024, **63**, e202410016.
- 34 T. Zhang, Z. Wu, Q. Gong, L. Qiu, Z. Wu, B. Zhong, Y. Chen, X. Guo, *Chem. Eng. J.*, 2025, **520**, 165464.
- 35 H. Liu, L. Xu, H. Tu, Z. Luo, F. Zhu, W. Deng, G. Zou, H. Hou, X. Ji, *Small*, 2023, **19**, 2301275. View Article Online
DOI: 10.1039/D6LF00021E
- 36 L. Xu, J. Li, L. Li, Z. Luo, Y. Xiang, W. Deng, G. Zou, H. Hou, X. Ji, *Small*, 2021, **17**, 2102978.
- 37 J. Yuan, H. Dong, B. Wang, M. Qiu, Z. Liu, X. Wu, S. Zhong, G. Tong, Z. Chen, J. Zhang, Q. Zhang, J. Zhu, X. Zhuang, *Chem. Eng. J.*, 2024, **487**, 150489.
- 38 Y. Zhang, J. Yu, H. Shi, S. Wang, Y. Lv, Y. Zhang, Q. Yuan, J. Liang, T. Gao, R. Wei, X. Chen, L. Wang, Y. Yu, W. Liu, *Adv. Funct. Mater.*, 2025, **35**, 2421054.
- 39 X. Li, S. Feng, C. Zhao, Q. Cheng, Z. Chen, S. Sun, X. Chen, X. Zhang, B. Li, J. Huang, Q. Zhang, *J. Am. Chem. Soc.*, 2022, **144**, 14638–14646.
- 40 Z. Yang, Z. Yu, Y. Qu, X. Wang, W. Lu, T. Li, N. Chen, M. Yao, P. Gao, D. Zhang, F. Du, *Chem. Eng. J.*, 2023, **477**, 147077.
- 41 Y. Wang, Q. Sun, J. Zou, Y. Zheng, J. Li, M. Zheng, Y. Liu, Y. Liang, *Small*, 2023, **19**, 2303344.
- 42 J. Zhang, Y. Zeng, Q. Li, Z. Tang, D. Sun, D. Huang, L. Zhao, Y. Tang, H. Wang, *Energy Storage Mater.*, 2023, **54**, 440–449.
- 43 P. Wang, J. Tan, Z. Liu, C. Wang, C. Bao, X. Xia, B. Li, Q. Liu, *Adv. Funct. Mater.*, 2025, e12441.
- 44 Y. Lu, C. Zhao, J. Huang, Q. Zhang, *Joule*, 2022, **6**, 1172–1198.
- 45 J. Chen, E. Quattrocchi, F. Ciucci, Y. Chen, *Chem*, 2023, **9**, 2267–2281.
- 46 C. Yu, J. Cho, J. Dunham, R. Ghahremani, K. Liu, P. Lindemann, Z. Garver, D. Barchiesi, R. Farahati, J. Kim, *J. Power Sources*, 2024, **597**, 234116.
- 47 D. Zhang, T. Tian, Y. Guo, J. Zhang, J. An, J. Hui, Y. Shi, P. Müller-Buschbaum, S. Yang, B. Li, *Adv. Funct. Mater.*, 2025, e24041.
- 48 L. Tang, B. Chen, Z. Zhang, C. Ma, J. Chen, Y. Huang, F. Zhang, Q. Dong, G. Xue, D. Chen, C. Hu, S. Li, Z. Liu, Y. Shen, Q. Chen, L. Chen, *Nat. Commun.*, 2023, **14**, 2301.
- 49 L. Qian, T. Or, Y. Zheng, M. Li, D. Karim, A. Cui, M. Ahmed, H. Park, Z. Zhang, Y. Deng, A. Yu, Z. Chen, K. Amine, *Renewables*, 2023, **1**, 114–141.



Data Availability Statement:

View Article Online
DOI: 10.1039/D6LF00021E

The authors confirm that the data supporting the findings of this study are available within the article and its ESI. Raw data that support the findings of this study are available from the corresponding author, upon reasonable request.

